IJICTR
International Journal of Information & Communication Technology Research

Volume 17- Number 3 – 2025 (1-8)

Inverse Design of a Wide-Angle Wideband Programmable THz Reflectarray Through Generative Adversarial Networks

Pezhman Yousefi
Department of Electrical and Information Engineering
Polytechnic University of Bari
p.yousefi1@phd.poliba.it

Ali Khajeh
School of Electrical and Computer Engineering
Shiraz University
Shiraz 71946, Iran
a.khajeh@shirazu.ac.ir

Alireza Yahaghi
School of Electrical and Computer Engineering
Shiraz University
Shiraz 71946, Iran
yahaghi@shirazu.ac.ir

Keyhan Hosseini*
Department of Electronics and Communication Engineering
Faculty of Engineering
University of Kurdistan
Sanandaj, Kurdistan 66177, Iran
k.hosseini@uok.ac.ir

Received: 12 September 2024 – Revised: 3 November 2024 - Accepted: 22 December 2024

Abstract—**A reflectarray optimized through a Generative Adversarial Network (GAN) is demonstrated. This design focuses on the impact of the top layer on the reflection phase and utilizes the correlation between phase distribution and the direction of the reflected beam. Six programmable subcells are optimized to accommodate two incident angle waves simultaneously. Silicon substrate is exploited making the design compatible with integrated circuits. The far-field analysis indicates that for incident angles of 19.471° and 41.81°, as well as their vicinity, the reflectarray effectively redirects the incoming waves to reflect towards near-normal direction to its surface. This suggests a near independence of the deflection angle from the incident angle within a specific angular range, making the proposed reflectarray a planar THz beam collimator. The proposed subcells achieve a reflection phase range of 342°. The return losses for the incident angles of 19.471° and 41.81° are 1.9 dB and 1.4 dB, respectively. For a finite reflectarray measuring 15λ×5λ, the pattern gain and fractional bandwidth are reported as 19.44 dB and 24.8% for the incident angle of 19.471°, and 19.17 dB and 29.9% for the incident angle of 41.81°. This denotes an excellent wideband behavior for the proposed single-layer pixelated reflectarray.**

Keywords: Reflectarray, Unitcell, Subcell, Deflection, Generative Adversarial Network.

Article type: Research Article

Publisher: ICT Research Institute

* Corresponding Author

I. INTRODUCTION

The terahertz (THz) band, spanning from 0.1 to 10 THz [1], has garnered significant attention due to its capabilities, including high data rates, high efficiency [2], and minimal fading. These attributes make it suitable for various applications such as sensing, imaging, screening, and time-domain spectroscopy. Current research trends in the THz domain encompass imaging systems utilizing aperture synthesis techniques [3], spectroscopy methods for explosive detection [4], electromagnetic interactions with biological materials [5], spectroscopic diagnostics [6], counter-terrorism efforts [7], analysis of additive content in polymeric materials [8], imaging of nucleobases and cancerous tissues [9], and future developments in imaging and sensing technologies [10].

Terahertz (THz) antennas [11] are a focal point of interest for numerous researchers due to their diverse applications stemming from the unique advantages of the THz frequency range. Various designs are currently under investigation, including fishnet-based metamaterial patch antennas [12], microstrip antennas utilizing synthesized photonic bandgap substrates [13], and those employing photonic bandgap materials [14]. Additionally, plasmonic antennas that incorporate graphene stacks [15], rectangular microstrip antennas constructed on dual-layer substrate materials [16], ultrawideband elliptical microstrip antennas [17], and super wideband hexagonal fractal antennas [18] represent significant areas of active research in the THz antenna domain. Reflectarray antennas, which consist of a printed layer positioned atop a grounded substrate, have emerged as a promising low-cost option for beam shaping [19, 20]. Within the category of reflectarrays, the principle of directing incident waves at a predetermined angle can be articulated through the progressive phase alterations occurring within the subcells of the reflectarray. The phase variations of these subcells are influenced by several factors, including delay or transmission line length, patch size [21], dielectric resonator height [22, 23], aperture size, and the properties of the underlying dielectric [24]. These parameters have demonstrated considerable utility in steering or shaping the reflected beam [25].

Two distinct designs for the manipulation of incident THz waves are presented in references [26], [27]. In [27], a reflectarray composed of resonant microstrip gold patches on a grounded PDMS dielectric substrate is engineered to redirect an incoming beam to a predetermined angle that is anomalous to the specular direction. A similar THz reflectarray is also proposed to differentiate between the two polarization components of a normally incident wave by specifically designing orthogonal paired sets of strip dipoles on a grounded substrate, aimed at the designated angles of $\pm 30°$ [27]. Additionally, within the THz spectrum, another design is introduced to project incident waves at various frequencies into non-specular angles [28]. However, due to the asymmetrical geometry of the cell, the polarization of the wave is not maintained. In a different design, a THz reflectarray is capable of deflecting three polarization-independent plane waves at different frequencies (0.7, 1.0, and 1.5 THz) to three distinct angles [29]. Nevertheless, this simultaneous dependence on both angle and frequency imposes undesirable constraints on the steering of the deflected waves

In this paper, we illustrate that through meticulous engineering of the upper layer utilizing Generative Adversarial Network (GAN) [30], it is possible to systematically generate a programmable reflectarray featuring pixelated unit cells capable of redirecting two incoming waves at distinct angles into a singular off-specular direction. The silicon-based reflectarray proposed exhibits a degree of independence from the angle of incidence within a specific range, offering a proper THz integrated-circuit-compatible beam collimator. To the best of the authors' knowledge, no comparable findings have been reported.

II. DEFLECTION PRINCIPLE

The previously mentioned reflection phase of subcells is contingent upon the specific characteristics of the structure, particularly the upper metallic layer and the dielectric substrate. In reflectarrays, the arrangement of the reflection phase distribution across the subcells allows for the shaping or deflection of the reflected beam to a designated angle. For the n^{th} subcell (n = 1, 2, …), the phase change Φ_n must adhere to the conditions outlined in [26], i.e.,

$$\Phi_1 + (n - 1)\, k_0\, d = \Phi_n, \tag{1}$$

The free space wavenumber, denoted as k_0, is defined as $2\pi/\lambda_0$, where λ_0 represents the wavelength. The variable d signifies the path difference between waves reflected from two neighboring subcells. This path difference can be articulated in relation to the deflection angle θ and the length of the subcell a, specifically as $d = a \sin\theta$. Consequently, the phase difference in reflection between adjacent subcells can be represented in the following manner [26]:

$$\Delta\Phi = \Phi_{n+1} - \Phi_n = k_0\, \Delta s = (2\pi/\lambda_0)\, a \sin\theta, \tag{2}$$

The phase difference between two adjacent subcells is denoted as ΔΦ. Consequently, the incident angle can be expressed in relation to the phase difference as follows:

$$\sin\theta = (\lambda_0\, \Delta\Phi)/(2\pi a), \tag{3}$$

In this paper, we investigate the incident angles that yield normal reflection, interpreting the deflection angle θ as the angle formed between the incident ray and the surface normal. The incident wave is assumed

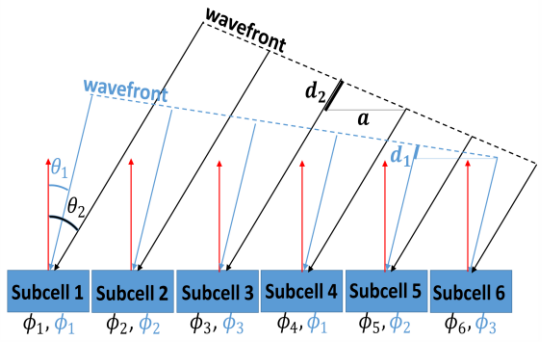

Figure 1. Proposed schematic of the eflectarray in normal reflection mode

to be the transverse electric (TE) mode, with the electric field perpendicular to the plane of incidence. The azimuthal angle is set to $\Phi = 0°$, consistent with the formulations in Section II.

The operational frequency is set at 1.5 THz, with a defined parameter of $a = \lambda_0/2 = 100$ µm. By assuming a cell that accommodates phase differences of $\Delta\Phi = 60^o$ and 120^o, we calculate the incidence angles using equation (3), resulting in $\theta_1 = \sin^{-1}(1/3) = 19.471°$ and $\theta_2 = \sin^{-1}(2/3) = 41.81°$, respectively. Fig. 1 illustrates a schematic representation of the problem. The total phase difference introduced by the cell ($n\Delta\Phi$), must equal the smallest multiple of 360°, where n represents the number of subcells. For phase differences of $\Delta\Phi = 60°$ and 120°, it is determined that six and three subcells are necessary, respectively. Consequently, each cell must incorporate six subcells to satisfy the phase difference requirement.

III. DESIGN DETAILS

The unit cell has been designed to accommodate plane waves with incident angles of $\theta = 41.81^o$ and 19.471^o, oriented normal to the surface. Consequently, two beams, each with distinct incident angles, will be redirected into a unified direction. By the principle of reciprocity, a wave incident normally will be separated into two reflective components directed towards the specified angles. Fig. 2 illustrates the unit cell, which consists of a 1×6 array of subcells.

Application of learning-based optimization algorithms to electromagnetic structures has led to a significant reduction in time consumption. The GAN optimization procedure, as detailed in [31], is implemented in MATLAB, with data retrieved from HFSS during each iteration. GAN represents a sophisticated deep learning framework which involves the training of two neural networks, i.e. generator and predictor, that engage in a competitive process to produce increasingly realistic new data derived from a specified training dataset. The term adversarial is used because the two networks operate in opposition to one another. The generative network is responsible for creating new data by altering an input sample to the greatest extent possible, while the predictor network's role is to assess whether the generated output is part of the original dataset. In other words, the generator network generates proper input geometrical dimensions, i.e. pixelated pattern of a cell, for a physical structure, while the predictor network evaluates the output, e.g. reflection phase, for the specified inputs. The network continues to refine the generated data until a specified error threshold is satisfied [31].

Unlike evolutionary algorithms, which require initial guess with issues concerning instability and possible divergence, GAN is an appropriate technique to model multifunctional structures with sophisticated unit cells. Pixelated reflectarrays possess many design parameters and this places them in the category of complex structures. The proposed reflectarray with two incident angles deflecting back along the normal direction, is a multifunctional device. On the other hand, the network's complexity in GAN is independent of the structure's complexity. In addition, GAN avoids

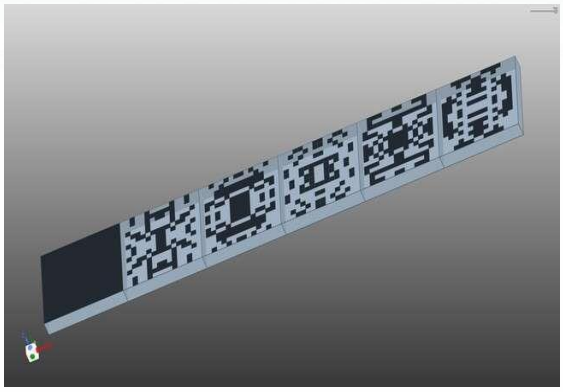

Figure 2. the coded reflectarray composed of six A unit cell of subcells

multiple solutions, which is common in inverse designs. Finally, GAN is able to design diverse structures based on limited inputs, making them suitable in designing pixelated reflectarrays [32].

By encoding the pixelated map of the reflectarray's subcells to images, each subcell undergoes a distinct GAN optimization process, resulting in two separate reflection phase distributions for each incident wave. The subcells are constructed from randomly arranged pixels of perfect electric conductor (PEC) situated on a grounded silicon substrate. The top layer, composed of these pixels, is represented by a binary string of 0s and 1s (1 indicating metal and 0 indicating no metal). It is assumed that each subcell contains 16×16 pixels, totaling 256. To maintain symmetry along both the vertical and horizontal axes of the surface and to alleviate computational demands, the optimization process randomizes 64 bits. An example of the fifth subcell is illustrated in Fig. 3, where one quarter of the subcell is optimized, allowing the remaining sections to be derived from this symmetry. Datasets of sizes 8000 and 3000 are exploited in the training and validation phases of GAN. Although this seems time consuming, it is performed once and could be utilized to design diverse multifunctional pixelated reflectarrays, other than the structure proposed in this paper.

A flowchart of the proposed learning-based algorithm is depicted in Fig. 4. Note that for the sake of simplicity, the surface of the first subcell is treated entirely as a PEC, as its reflection phase for any angle of incidence is consistently -180^o. This is depicted in Fig. 2. Accordingly, only pixelated subcells have to go under the GAN-based optimization. Therefore, for two incident angles, ten desired phases are considered as the targets. Accordingly, the network has 64 inputs and 10 outputs. Table I shows the desired phases. Mean square error criterion is utilized to evaluate the performance of the GAN optimization algorithm, defined as

$$MSE = [\Sigma^{n}_{i=1} (\Phi_{id} - \Phi_{io})^2]/n, \quad (4)$$

where n is the number of reflection phases (for this design n = 10). In addition, Φ_{id} and Φ_{io} are the desired and optimized phases of the pixelated subcells. The error threshold is set to 0.05, when the phases are calculated in radians.

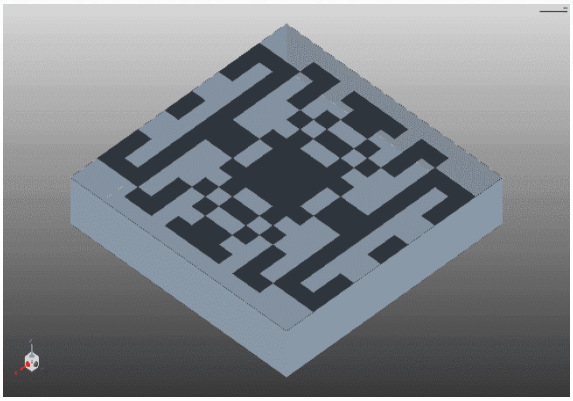

Figure 3. The symmetric arrangement of pixels in the fifth subcell

TABLE I. REFLECTION PHASES OF THE SUBCELLS IN DEGREES

θ	Φ_1	Φ_2	Φ_3	Φ_4	Φ_5	Φ_6
19.47	-180	-120	-60	0	60	120
19.47	-180	-120.3	-60.6	-1.7	61.6	123.4
41.81	-180	-60	60	180	-60	60
41.81	-180	-59.5	60.8	-178.9	-60.7	62.2

* White and shaded rows correspond to desired and optimized reflection phases, respectively.

The silicon substrate with the refractive index n = 3.42 and extinction coefficient κ = 0.00006 has a thickness of h = 15 μm. Silicon substrate makes the design compatible with integrated circuit technology. As previously stated, the length of the subcells is a = 100 μm, resulting in each square pixel measuring 100/16 = 6.25 μm. For incidence angles of θ = 19.47° and 41.81°, the second subcell is expected to demonstrate reflection phases of -120° and -60°, which are determined during the optimization process as -120.3° and -59.5°, respectively. The optimized reflection phases for all subcells are presented in Table I, with values expressed in degrees. The difference between the desired and optimized values can be reduced to an acceptable level by relaxing the symmetry constraint and increasing the number of pixels involved in the optimization. Alternatively, symmetry can be maintained by augmenting the number of pixels in one-quarter of the cell illustrated in Fig. 3. In either scenario, the computational demands will increase. In contrast to conventional learning based routines, GAN is capable of learning the performance of multifunctional structures.

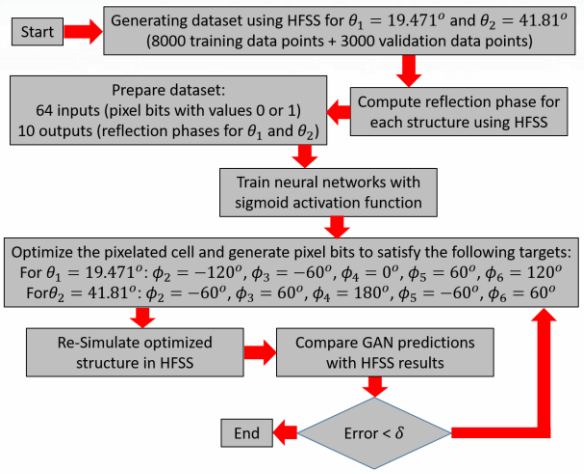

Figure 4. Flowchart for the GAN-based optimization of the pixelated subcells to satisfy the desired reflection phases.

IV. RESULTS AND DISCUSSIONS

The structure is modeled using Ansys HFSS software in conjunction with GANs. Floquet ports are utilized to stimulate the periodic reflectarray, while primary-secondary boundaries are established to define the characteristics of the unit cell. Fig. 5a illustrates the 2D far-field reflection patterns for the two principal beams at angles θ_1 = 19.47° and θ_2 = 41.81°, demonstrating that the peak power of the beam is oriented towards the normal direction.

Fig. 5b illustrates the reflection patterns corresponding to incident angles ranging from 15° to 50°, with increments of 5°. Table II presents the magnitudes of the reflected main beams, normalized to those of θ_1, along with their angular deviations from the normal. The incidence angles near θ_1 and θ_2 exhibit reflections that are directed close to the normal. This indicates a reflection behavior that is largely independent of the angle. However, as the incidence angles move further away from these two primary angles, the deviations from the normal become more pronounced. From Table II, a similar behavior is observed for the normalized magnitudes of the beams in terms of deviation from the primary angles. Notably, no grating lobes are detected in any of the scenarios.

Increasing the number of unit cells allows for a greater variety of phase shifts among the subcells. Consequently, this enables the simultaneous manipulation of more than two primary incidence angles with normal reflection. If the angular separation between these primary angles remains relatively small, all surrounding angles will produce near-normal reflections. This development could lead to a practical angle-independent reflectarray capable of directing incident beams within a specified angular range towards the normal direction. This may find applications in beam collimators.

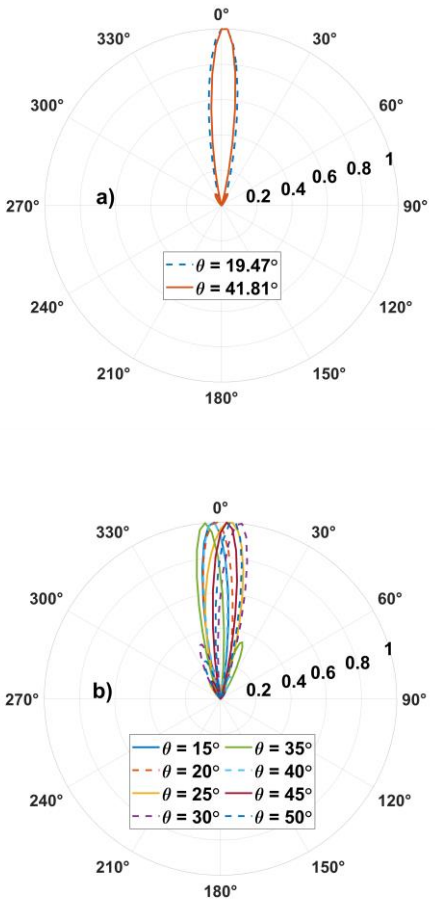

Figure 5. Far-field reflection patterns of the infinite periodic reflectarray at a) primary angles, b) nearby angles. θ is measured from z-axis

Fig. 6 depicts snapshots of the reflected electric field from a unit cell of the programmable reflectarray for the incident angles 19.47°, 41.81°, 30°, and 15°. An almost pure normally propagating reflected plane wave is evident from the figure. In agreement with Table II and Fig. 5, a little distortion in the planar wavefront and deviation from the normal angle of reflection is observed for the incident angles 30° and 15°. This is due to the contribution of reflected waves propagating in spurious angles.

Fig. 7 illustrates the reflection phases of the proposed unit cell for the incident angles θ_1 and θ_2 as a function of frequency, covering a range of 342° for both angles. Additionally, the reflection amplitudes are depicted in the same figure. Accordingly, at the designated frequency of 1.5 THz, the return losses for angles θ_1 and θ_2 are recorded at 1.9 dB and 1.4 dB, respectively. Consequently, the less oblique incidence angle θ_1 results in reduced return losses due to its diminished interaction with the silicon substrate. The reflection amplitude and phase of the periodic reflectarray, depicted in Fig. 7, are computed utilizing a Floquet port of the same aperture as the unit cell. The

port is excited at two different angles 19.471° and 41.81° using primary-secondary boundaries defined in HFSS. The loss of the reflectarray unit cell would thus be equal to the return loss of the Floquet port. Note that from reciprocity, when the proposed reflectarray is

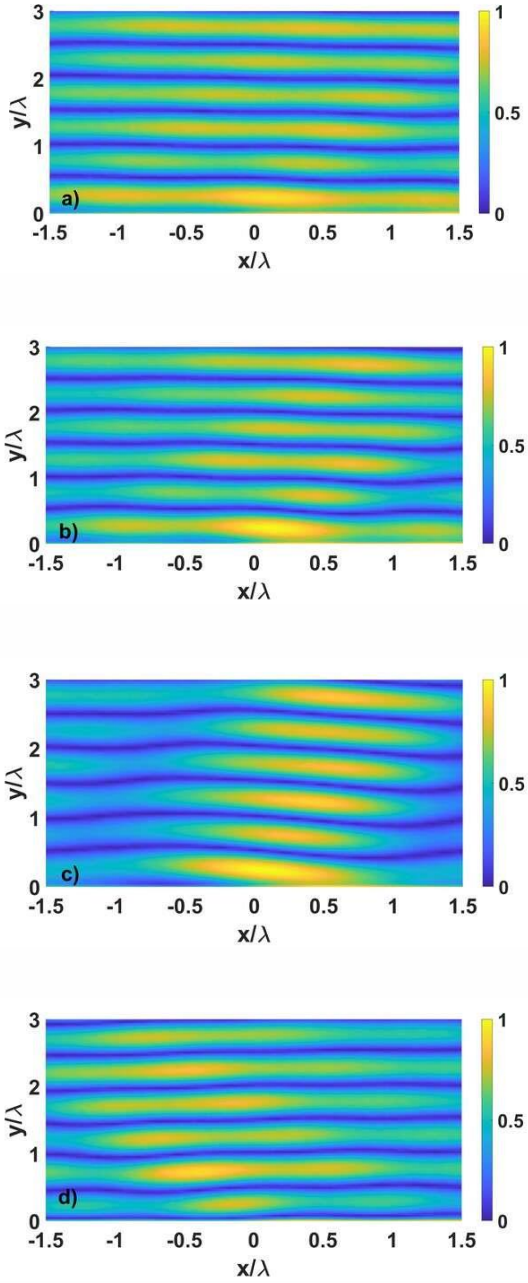

Figure 6. Snapshots of the reflected electric field distribution from the programmable reflectarray for the incident angles a) 19.47°, b) 41.81°, c) 30°, and d) 15°.

illuminated by the aforesaid angles, it will generate a reflection beam normal to its surface.

As the frequency becomes smaller than the design frequency, the incident wave will gradually treat the unit cell as a bulk composite with an effective electric permittivity. In this case, the return loss approaches values around 0 dB since no resonance will occur between the wave and a cell with a very small electric size. On the other hand, for frequencies much larger than the design frequency higher order resonances may arise at some discrete resonance frequencies which result in pronounced return losses at the corresponding frequencies. Since such resonances are far from the desired frequency range, they are of no interest and not considered when designing a reflectarray.

A finite form of the reflectarray under consideration is simulated in HFSS. It is designed with a configuration of 30 subcells in length and 10 subcells in width, resulting in a total of 300 subcells. Each cell measures 3λ by 0.5λ and thus the size of the reflectarray amounts to 15λ by 5λ. The power radiation pattern is characterized by a $\cos^n(\theta)$ profile, with n = 12, to mimic the pattern of a transmitting horn antenna. The reflection patterns corresponding to the two primary incident angles, θ_1 and θ_2, are illustrated in Fig. 8a. Compared to Fig. 5, there is a slight deviation of the main beams from the broadside, accompanied by a more pronounced appearance of sidelobes. An increase in the number of simulated cells is expected to enhance the results. Fig. 8b presents the radiation patterns for the primary angles, and also θ = 15°, and 50°. A clear near-normal reflection is evident. Lastly, Fig. 9 depicts the pattern gains for θ_1 and θ_2, which exhibit nearly identical characteristics. The gains at the central frequency are measured at 19.44 dB for θ_1 and 19.17 dB for θ_2. The 3-dB fractional gain bandwidths are reported to be 24.8% and 29.9%, respectively.

TABLE II. NORMALIZED MAGNITUDE AND DEFLECTION ANGLE OF THE REFLECTED BEAMS

θ	15	**19.47**	20	25	30
G_n	0.91	**1**	0.95	0.9	0.87
Δθ	-2	**0**	-1	3	7
θ	35	40	**41.81**	45	50
G_n	0.88	0.97	**0.97**	0.94	0.85
Δθ	-5	-1	**0**	2	4

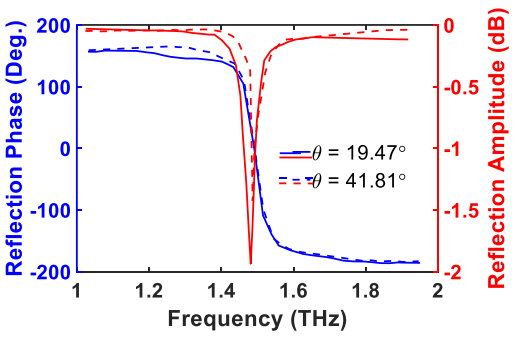

Figure 7. Reflection phases and reflection amplitudes of the unit cell in terms of frequency for the two primary incident angles.

Table III compares the performance factors for the proposed coding reflectarray and similar works in the literature. Due to challenges in realization process, there are not as much THz reflectarrays in the literature as GHz reflectarrays. Except for [36], which operates at GHz band, the proposed reflectarray exhibits a superior 3-dB fractional gain bandwidth over other works in the table. It is interesting that such a high bandwidth is achieved with a small substrate thickness of $h = 0.075\lambda_0$ at the central frequency 1.5 THz. In contrast to many works in the table, the proposed reflectarray benefits from a single layer structure which simplifies its fabrication at the challenging THz band. The gain corresponding to the aperture size of each structure is also reported, wherein the proposed structure shows acceptable gain at the frequency of operation. The total phase coverage of the proposed pixelated unit cell is 342^0 (close to the full cycle), which is satisfactory. The small substrate thickness is a reason for the achieved phase coverage. However, the proposed cell suffers from a bit high return loss, which is attributed to strong resonances caused by the small thickness of the substrate. The loss may be decreased by increasing the thickness of the substrate. The advantage of the pixelated cell over other cells is its reprogramming ability to obtain other functionalities.

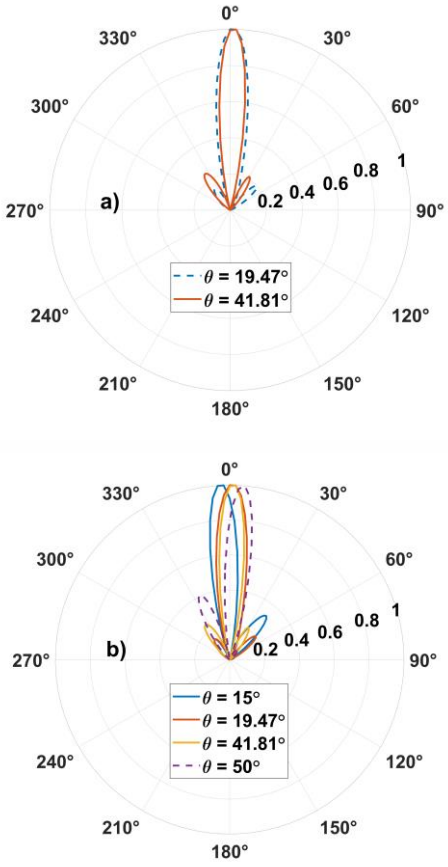

Figure 8. Far-field reflection patterns of the simulated finite reflectarray at a) primary angles, b) nearby angles

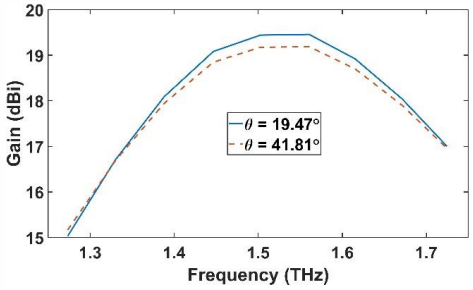

Figure 9. Gain of the simulated reflectarray for the two primary incident angles.

V. CONCLUSIONS

A programmable terahertz (THz) reflectarray is introduced that simultaneously directs two incoming beams towards the normal direction. The deflection law is utilized to establish a relationship between the phase shifts of the cells and the angles of incidence. Subsequently, a generative adversarial network (GAN) is employed to design the pixelated subcells of the unit cells. The proposed reflectarray may be utilized as a wideband THz silicon-based beam collimator. Future work will involve incorporating loss and thickness into the pixelated cells by utilizing a metal such as gold or silver. The loss induced by such metals is a challenge to devise a converged algorithm in both learning- and non-learning-based approaches. Furthermore, by offering additional design angles, we aim to develop an angularly-stable reflectarray capable of directing beams over a sufficiently large angular range into the normal or any specified reflection direction. This objective can be achieved by systematically adjusting the proposed GAN-based approach.

TABLE III. COMPARISON OF THE PERFORMANCE FACTORS OF THE PROPOSED CODING REFLECTARRAY WITH SIMILAR WORKS.

Ref.	DP	f_0	CT	h (λ_0)	NL	MRL (dB)	TPR (°)	AS (λ_0^2)	Gain (dBi)	FBW (%)
[26]	2013	1 THz	Gold Patch	0.05	1	1.2	330	168×168	NG	NG
[27]	2014	1 THz	Orthogonal Dipole Resonators	0.067	1	5.5	300	168×168	NG	3
[29]	2016	0.7 THz 1 THz 1.5 THz	Cross and Parasitic Dipoles	0.035 0.05 0.075	4	1.9 1.8 1.6	270 270 270	23.3×23.3 33.3×33.3 50×50	NG	NG
[33]	2021	10 GHz	Minkowski Fractal	0.34	2	0.25	740	6.8×5.2	26.8	2.5
[34]	2023	30.5 GHz	1bit (Dipole & End Stubs)	0.15	1	0.1	140	6×6	21.5	29.5
[35]	2019	29 GHz	2bit (PIN Diode & Vias)	0.125	6	1.6	315	7×7	19.8	16.2
[36]	2022	90 GHz	1bit (Random Cut-Wire Resonators)	0.1	1	0	350	10.2×10.2	NG	66.7
[37]	2025	7.5 GHz	1bit (PIN Diode & Polarizer)	0.188	3	0.5	180	4.5×4.5	7.5	8
[38]	2022	5.2 GHz	1bit (Patch & Varactor Diodes)	0.051	3	4.7	280	10.4×10.4	26	NG
[39]	2023	0.9 THz	Metal-Only Stack	1.17	9	1	360	36.48×36.48	35.96	26.67
[40]	2018	1.52 THz	Graphene Patch	0.132	1	1	360	3.88×3.88	15	19.73
TW	2025	1.5 THz	1bit (Pixelated)	0.075	1	1.9	342	15×5	19.44	29.9

* TW: This Work, DP: Date of Publication, CT: Cell Type, CS: Cell Size, h: Substrate Thickness, NL: Number of Layers, MRL: Maximum Return Loss, TPR: Total Phase Range, Pol: Polarization, AS: Aperture Size, FBW: Fractional Bandwidth, NG: Not Given.

REFERENCES

[1] Federici, J. and L. Moeller, Review of Terahertz and Subterahertz Wireless Communications. Journal of Applied Physics, 2010. 107(11): p. 111101.

[2] Vettikalladi, H., et al., Sub-THz Antenna for High-Speed Wireless Communication Systems. International Journal of Antennas and Propagation, 2019. 2019(1): p. 9573647.

[3] Li, X., et al., High-Throughput Terahertz Imaging: Progress and Challenges. Light: Science & Applications, 2023. 12(1): p. 233.

[4] Bhumika, S. and a. Ranu Gadi, Analytical Tools and Methods for Explosive Analysis in Forensics: A Critical Review. Critical Reviews in Analytical Chemistry, 2025. 55(2): pp. 251-277.

[5] Liu, L., et al., Interactions Between Electromagnetic Radiation and Biological Systems. iScience, 2024. 27(3).

[6] Vaks, V., et al., High‐Resolution Terahertz Spectroscopy for Medical Diagnostics. Journal of Biophotonics, 2024: p. e202400316.

[7] Scalici, M. and P. Livreri, A Novel Plasmonic Nanoantenna-Based Sensor for Illicit Materials and Drugs Detection. IEEE Sensors Journal, 2024. 24(17): pp. 27051-27060.

[8] Brodie, C.H., I. Spotts, and C.M. Collier, Terahertz Components By Additive Manufacturing: Material and Fabrication Characterizations Realized Through Bragg Structures. IEEE Transactions on Terahertz Science and Technology, 2024. 14(5): pp. 745-757.

[9] Pu, Z., et al., A New Horizon for Neuroscience: Terahertz Biotechnology in Brain Research. Neural Regeneration Research, 2025. 20(2): pp. 309-325.

[10] Jiang, W., et al., Terahertz Communications and Sensing For 6G and Beyond: A Comprehensive Review. IEEE Communications Surveys & Tutorials, 2024. 26(4): pp. 2326-2381.

[11] Elalaouy O., and El Ghzaoui M. , THz Antennas: Applications and Challenges---A Review , bookTitle= Next Generation Wireless Communication: Advances in Optical, mm-Wave, and THz Technologies. 2024, Cham: Springer Nature Switzerland. pp. 235-249.

[12] Y, D.S., C.K. Akin, and C. Sabah, Fishnet Based Metamaterial Loaded THz Patch Antenna. Optical and Quantum Electronics, 2016. 48(2): p. 168.

[13] Temmar, M.N.E., et al., Analysis and Design of a Terahertz Microstrip Antenna Based on a Synthesized Photonic Bandgap Substrate using BPSO. Journal of Computational Electronics, 2019. 18(1): pp. 231-240.

[14] Aly, A.H. and F.A. Sayed, THz Cutoff Frequency and Multifunction Ti 2Ba2Ca2Cu3O10/GaAs Photonic Bandgap Materials. International Journal of Modern Physics B, 2020. 34(10): p. 2050091.

[15] D, K., R. Kavitha, and J.V. Anchitaalagammai, A Graphene Based Multi-Band Antenna Array for Next Generation IoT Networks in THz Spectrum. Physica Scripta, 2025. 100(3): p. 035543.

[16] PourHosseini, M., et al., High Gain Multi-Band Circularly Polarized Bi-Layered Metasurface Patch Array Antenna with Dual-Orthogonal Feeds. Optical and Quantum Electronics, 2025. 57(2): p. 155.

[17] Singhal, S., Ultrawideband Elliptical Microstrip Antenna for Terahertz Applications. Microwave and Optical Technology Letters, 2019. 61(10): pp. 2366-2373.

[18] Sarthak, S. and Jaiverdhan, Hexagonal Fractal Antenna for Super Wideband Terahertz Applications. Optik, 2020. 206: p. 163615.

[19] Chang, D.C. and M.C. Huang, Microstrip Reflectarray Antenna with Offset Feed. Electronics Letters, 1992. 28 (16) pp. 1489-1491.

[20] Yousefi, P., et al., RHC-Based Systematic Design of a Wide-Angle Periodic Coded THz Reflectarray. in 2024 11th International Symposium on Telecommunications (IST), IEEE, 2024. pp. 1-5.

[21] Carrasco, E., M. Barba, and J. Encinar, Aperture-Coupled Reflectarray Element with Wide Range of Phase Delay. Electronics Letters, 2006. 42: pp. 667 - 668.

[22] Nayeri, P., et al., 3D Printed Dielectric Reflectarrays: Low-Cost High-Gain Antennas at Sub-Millimeter Waves. IEEE Transactions on Antennas and Propagation, 2014. 62(4): pp. 2000-2008.

[23] Keller, M.G., et al., A Ka-Band Dielectric Resonator Antenna Reflectarray. 2000. pp. 1-4.

[24] Huang, J. and J.A. Encinar, Practical Design Approach. 2008. pp. 79-92.

[25] Hosseini, K. and Z. Atlasbaf, PLRC-FDTD Modeling of General GSTC-Based Dispersive Bianisotropic Metasurfaces. IEEE

Transactions on Antennas and Propagation, 2018. 66(1): pp. 262-270.
[26] Tiaoming, N., et al., Experimental Demonstration of Reflectarray Antennas at Terahertz Frequencies. Opt. Express, 2013. 21(3): pp. 2875-2889.
[27] Tiaoming, N., et al., Terahertz Reflectarray as a Polarizing Beam Splitter. Opt. Express, 2014. 22(13): pp. 16148-16160.
[28] Qu, S.-W., et al., Controlling Dispersion Characteristics of Terahertz Metasurface. Scientific Reports, 2015. 5(1): pp. 9367.
[29] Hasani, H., et al., Tri-Band, Polarization-Independent Reflectarray at Terahertz Frequencies: Design, Fabrication, and Measurement. IEEE Transactions on Terahertz Science and Technology, 2016. 6(2): pp. 268-277.
[30] Gonog, L. and Y. Zhou, A Review: Generative Adversarial Networks. 2019. pp. 505-510.
[31] Goodfellow, I.J., et al., Generative Adversarial Nets, Z. Ghahramani, et al., Editors. 2014.
[32] An, S., et al., Multifunctional Metasurface Design with a Generative Adversarial Network. Advanced Optical Materials, 2021. 9(5): p. 2001433.
[33] Ozturk, E. and B. Saka, Multilayer Minkowski Reflectarray Antenna with Improved Phase Performance. IEEE Transactions on Antennas and Propagation, 2021. 69(12): pp. 8961-8966.
[34] Bashir, G., A.K. Singh, and A.A. Dubey, Wide Band Beam Steering Digital Metasurface Reflectarray Antenna for Millimeter Wave Applications. IEEE Access, 2023. 11: pp. 121800-121810.
[35] Diaby, F., et al., 2-Bit Reconfigurable Unit-Cell and Electronically Steerable Transmitarray at Ka-Band. IEEE Transactions on Antennas and Propagation, 2019. 68(6): pp. 5003-5008.
[36] Al-Nuaimi, M.K.T., et al., Coding Engineered Reflector for Wide-Band RCS Reduction Under Wide Angle of Incidence. IEEE Transactions on Antennas and Propagation, 2022. 70(10): pp. 9947-9952.
[37] Chan, C.H., et al., A Single-Bit Reconfigurable Folded Reflectarray/Transmitarray Antenna. IEEE Open Journal of Antennas and Propagation, 2025.
[38] Sayanskiy, A., et al., A 2D-Programmable and Scalable Reconfigurable Intelligent Surface Remotely Controlled via Digital Infrared Code. IEEE Transactions on Antennas and Propagation, 2022. 71(1): pp. 570-580.
[39] Miao, Z.W., A 1.0-THz High-Gain Metal-Only Transmit-Array Antenna Based on High-Precision UV-LIGA Microfabrication Technology. IEEE Transactions on Terahertz Science and Technology, 2022. 14(2): pp. 269-282.
[40] Deng, L., Wide-Band Circularly Polarized Reflectarray using Graphene-Based Pancharatnam-Berry Phase Unit-Cells for Terahertz Communication. Materials, 2018. 11(6): p. 956.

Pezhman Yousefi received his B.Sc. degree in Electrical Engineering from the University of Kurdistan, Iran, in 201٦. He received his M.Sc. degree in Telecommunication–Fields and Waves from Shiraz University, Iran, in 2020, where his research focused on reflect array antennas. Since April 2023, he has been pursuing his Ph.D. degree in Integrated Optics and Photonic Design at Politecnico di Bari, Italy, and is currently undertaking a research internship at the University of Aveiro, collaborating with PICadvanced, a company based in Portugal. His research interests include Integrated Photonics, Grating Couplers, and Nonlinear Optical Devices.

Ali Khajeh received his B.Sc. degree in Electrical Engineering with a focus on Telecommunications from the University of Sistan and Baluchestan in 2015. He then received his M.Sc. degree in Electrical Engineering with a specialization in Electromagnetic Fields from Shiraz University in 2020. His Master's research focused on Linear Converters Based on Graphene Metasurfaces.

Alireza Yahaghi received his B.Sc. degree in electrical engineering from the University of Tehran, Tehran, Iran, in 2002, the M.Sc. degree in fields and waves communication engineering from the Iran University of Science and Technology, Tehran, in 2004, and the Ph.D. degree from Shiraz University, Shiraz, Iran, in 2010, where he is currently a full-time Assistant Professor with the Department of Communication and Electronics Engineering. From 2008 to 2009, he was with the Laboratory for Electromagnetic Fields and Microwave Electronics (IFH), ETH Zürich, Zürich, Switzerland, as an Academic Guest. From 2014 to 2016, he was an Alexander von Humboldt Researcher with the Ultrafast Optics and X-Rays Division, CFEL, DESY, Hamburg, Germany. His research interests include numerical methods in Electromagnetics And Optics, Metamaterials and Metasurfaces, Plasmonics, and Transformation Optics.

Keyhan Hosseini received his B.Sc. degree in Electrical Engineering from the University of Tehran in 2010, and M.Sc. and Ph.D. degrees in Communication Engineering from Tarbiat Modares University (TMU), Tehran, Iran, in 2013 and 2018, respectively. Since 2020, he has been an Assistant Professor with the University of Kurdistan, Sanandaj, Iran. His research activity is focused on Metasurfaces, Optical Sensors and Absorbers, and Nanophotonics.